ORIGINAL PAPER

Foliation Effects on Mechanical and Failure Characteristics of Slate in 3D Space Under Brazilian Test Conditions

Changdong Ding[1,2,3] · Yang Zhang[4] · Dawei Hu[1,2] · Hui Zhou[1,2] · Jianfu Shao[3]

Abstract

Slate frequently encountered in numerous engineering applications basically exhibits significant anisotropies in terms of physico-mechanical properties due to the presence of well-developed foliation structures. The objective of this study is to investigate the mechanisms of foliation effects on the mechanical and failure characteristics of slate in three-dimensional (3D) space under Brazilian test conditions. A series of laboratory tests are conducted on slate with seven different foliation angles (φ), which are defined as the angle between the foliation plane and end surfaces of the specimen. On the basis of each foliation angle, five different loading angles (θ), which are defined as the projection of the angle between the loading surface and the foliation plane on the front side of the specimen, are selected to ensure that 3D space is involved. The high-speed camera and acoustic emission (AE) system are employed to analyse the failure characteristics of slate during loading process. The testing results indicated that the variations of applied failure force (AFF) with respect to loading angle (θ) significantly differ under varied foliation angles. With increase of foliation angle, the anisotropy ratio of the maximum to minimum AFF shows an increasing trend, suggesting that the anisotropy becomes more notable. The high-speed camera visually recorded the initiation and propagation of cracks. The specimen failure can involve two major processes: the local cracks first occurred on the disc flank, and then the fully connected cracks were formed causing the overall failure. The rupture evolution process inside the specimen was characterised by AE energy and AE hits, which was in good agreement with the high-speed camera observations. When the foliation angle is small, i.e. $0° \leq \varphi \leq 15°$, or large, i.e. $75° \leq \varphi \leq 90°$, the macro-cracks on both sides (i.e., front and back) show similarity to some certain, and the fracture patterns can be considered as two-dimensional (2D). However, when φ is in the range of 30°–60°, the fractured surfaces have 3D spatial distribution characteristics, and the macro-cracks appearing on both sides exhibit an approximately anti-symmetric relationship. It is also revealed that both φ and θ have significant effects on the AFF and the fracture patterns. The results are likely to provide experimental basis for further improving the theory of tensile properties of anisotropic rocks.

Keywords Anisotropic slate · Brazilian test · Foliation effects · Rock mechanics · Failure characteristics · Three-dimensional (3D) space

1 Introduction

Slate is a typical rock characterised with significant anisotropies in terms of physico-mechanical properties, which has become a hot topic over the recent years (Amann et al. 2012; Kim et al. 2012; Gholami and Rasouli 2014; Shen and Shao 2015; Garcia-Fernandez et al. 2019; Xia et al. 2020). The rock anisotropies are attributed to the foliation structure formed by orientated arrangement of mineral components under high temperature and high pressure (Ho et al. 2001; Delle Piane et al. 2015; Ding et al. 2020). Layered or foliated rocks, similar to slate, are frequently encountered in various engineering applications, and their anisotropic

✉ Dawei Hu
  dwhu@whrsm.ac.cn

1 State Key Laboratory of Geomechanics and Geotechnical Engineering, Institute of Rock and Soil Mechanics, Chinese Academy of Sciences, Wuhan 430071, China

2 University of Chinese Academy of Sciences, Beijing 100049, China

3 University of Lille, LaMcube, CNRS FRE2016, 59000 Lille, France

4 CNPC Engineering Technology R&D Company Limited, Beijing 102206, China

characteristics with respect to the mechanical behaviours are critical for engineering design and construction, especially in case of tensile properties. Rock materials usually have lower tensile strength in comparison with their compressive strength, and are easy to fail when subjected to tensile stress. Hence, the tensile strength is an important indicator in many engineering applications, e.g., exploitation of oil and gas resources (Al-Bazali et al. 2005; Masri et al. 2014; Wang et al. 2016), excavation of underground engineering (Everitt and Lajtai 2004; Lisjak et al. 2016; Zhou et al. 2016; Winn et al. 2019), geological disposal of radioactive waste in clay formations (Tsang et al. 2012; Valente et al. 2012; Hu et al. 2013), and construction of high-speed railways (Xu et al. 2018). Therefore, it is critically important to understand the mechanical properties and failure characteristics of rock materials under tensile stress.

The Brazilian test is an important method for indirectly measuring the tensile strength of rocks and other brittle materials (Carneiro and Barcellos 1953; Jaeger et al. 2009; Li and Wong 2013), which is easy to conduct in the laboratory and widely applied in rock engineering. In general, the tensile strength is lower when the loading direction is parallel to the weakness plane, and it is higher when the loading direction is perpendicular to the weakness plane (Debecker and Vervoort 2009; Vervoort et al. 2014; Mokhtari and Tutuncu 2016; Wang et al. 2018). However, some studies have documented that the tensile strength exhibits undulatory trend (Vervoort et al. 2014; Zhang et al. 2018), increasing first and then decreasing with increase in the weakness plane angle (Dan et al. 2013; Park and Min 2015; Roy and Singh 2016), and some other trends (Barla 1974; Chen et al. 1998; Bohloli et al. 2002; Tavallali and Vervoort 2010a). The tensile properties of nine different transversely isotropic rocks were studied by Vervoort et al. (2014), and four different trends in variation of the relative failure load as a function of inclination angle were summarized (see Fig. 1). In addition, Gholami and Rasouli (2014) found that there is no apparent relationship between the anisotropy angle and tensile strength of slate, and increasing water saturation can decrease the tensile strength. The failure modes of transversely isotropic rocks in Brazilian tests are mainly based on the following two viewpoints: (1) classification into layer activation, central fracture, and non-central fracture according to the crack shapes (Tavallali and Vervoort 2010a, b, 2013; Basu et al. 2013; Xu et al. 2018); (2) classification into tensile failure, shear failure, and mixed-mode failure according to the mechanical mechanisms (Chen et al. 1998; Dan et al. 2013; Vervoort et al. 2014; Tan et al. 2015; Wang et al. 2016; Zhang et al. 2018). Furthermore, many studies are focused on the fracture evolution of specimens in Brazilian tests by means of digital or high-speed camera (Debecker and Vervoort 2009; Wong and Jong 2014; Xu et al. 2018), acoustic emission (Wang et al. 2016; Zhang et al. 2018;
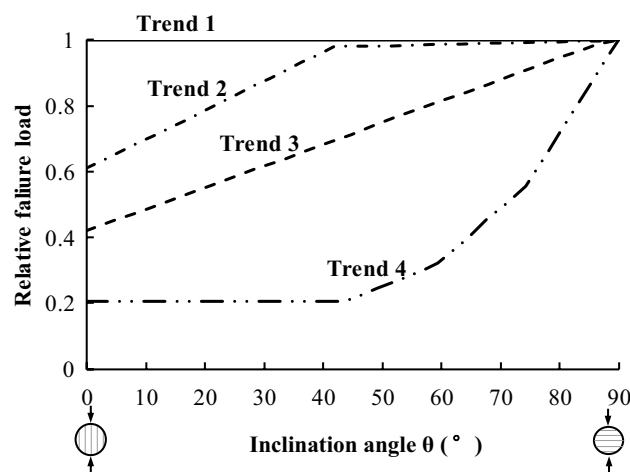
Fig. 1 Four different trends in variation of the relative failure load as a function of the inclination angle (Vervoort et al. 2014)

Xu et al. 2018), and digital imaging correlation (DIC) (Yin and Yang 2018; Yang et al. 2019). Tavallali and Vervoort (2010a) conducted Brazilian tests for layered sandstone and discussed the correlations between tensile strength, fracture length and the applied energy. Hu et al. (2017) analysed the failure mechanisms of interbedded sandstone by means of scanning electron microscope (SEM). Qiu et al. (2017) carried out dynamic Brazilian tests on the phyllite using the split Hopkinson pressure bar (SHPB) system to study the effects of dip angle on dynamic tensile strength. Ma et al. (2018) reviewed the results of the Brazilian tests for a large number of anisotropic rocks, and proposed new theoretical analysis methods to reveal the failure mechanisms and predict the tensile strength.

With rapid development of computational geomechanics, numerical simulation methods, such as UDEC (Tan et al. 2015), FEM/DEM (Cai and Kaiser 2004; Liu et al. 2019), and PFC (Duan and Kwok 2015; Xu et al. 2018; Ma and Huang 2018; Wang et al. 2018; Yang et al. 2019), are widely used to study the macro–micro mechanical properties of rocks, which play an important role in revealing the failure process (i.e., crack initiation, propagation and coalescence) and explaining the generation mechanisms of the fracture patterns.

The above researches mainly considered the effects of loading direction on tensile strength. The analyses of the fracture patterns were generally based on 2D hypothesis. It was assumed that the macro-cracks appeared on both sides of the disc have obvious similarities. However, little attention has been paid to the foliation effects in 3D space, i.e. coupling of the foliation angles and loading direction. Dan et al. (2013) carried out the Brazilian tests on four different rocks (e.g., one sandstone, two gneiss, and one slate) ranging from nearly isotropic to anisotropic, indicating that the

foliation angles have a great influence in all the gneiss and slate through a large number of tests and statistical analyses. Tavallali and Vervoort (2010a) also declared that the fracture patterns in most of the samples are similar on both sides and can mostly be considered as 2D. However, the fracture patterns in a few samples are true 3D, showing that the macro-cracks are significantly different on both sides of the sample. The authors hold that the combined effects of foliation angles and loading direction make the cracks on both sides of the disc different, that is, the 3D spatial effects of foliation plane. At present, it is difficult to reach a consensus on the strength and failure behaviour of transversely isotropic rocks in Brazilian tests, which may be due to neglecting the influences of foliation angles. Therefore, the Brazilian tests of slate in this context were conducted considering the coupling effects of foliation angles and loading direction. The failure process of each specimen, including crack initiation, propagation and coalescence, was recorded by a high-speed camera in real time, and AE system was employed to capture the rupture evolution process inside the specimen. The influences of foliation angles and loading direction on the mechanical and failure characteristics were discussed. The results may provide new insights and reference for analysis of tensile properties of transversely isotropic rocks.

2 Materials and Methods

2.1 Preparation of Slate Specimen

The studied slate with strong foliation structures was sampled from outcrops in Jiujiang, Jiangxi Province, China (see Fig. 2). Cylindrical cores with diameter of 50 mm were first drilled from one slate block along different directions with respect to foliation plane. According to the ISRM-suggested methods (ISRM 1978), the dimensions of the obtained specimens are 50 mm in diameter and 25 mm in thickness. The parallelism of the upper and lower surfaces is controlled within ± 0.5 mm, and the flatness of the surfaces is controlled within ± 0.1 mm.

The rock powders were collected for X-ray diffraction (XRD) during drilling of the specimens, and the results indicated that the studied slate mainly contains quartz (33.62%), chlorite (29.91%), muscovite (23.27%), albite (10.04%), and a small amount of illite (3.16%). To better understand the mineral composition, particle size and microstructure of slate, the thin section identification of internal foliation planes were further performed under the German Leitz-ORTHOPLAN polarizing microscope at 200 times magnification (see Fig. 3a). The directional arrangement of muscovite, chlorite and other minerals can be clearly observed. The Quanta 250 scanning electron microscope (SEM) with magnification of 800 times and 2000 times was used to observe the microscopic structures (see Fig. 3b, c). These SEM images show that the minerals have obvious scale crystalloblastic texture and directional arrangement of flaky minerals, such as sericite, chlorite and illite. The above mineral characteristics make the slate showing obvious foliation structures in macro-scale, which results in significant anisotropies in mechanical and thermal properties of slate in parallel and perpendicular to the direction of foliation (Ding et al. 2020).

2.2 Experimental Method and Procedure

As mentioned above, the 3D spatial effects of foliation plane are in consideration of both foliation angle and loading angle in Brazilian tests. In this context, the foliation angle is defined as the angle between the foliation planes and end surfaces of the specimen, as denoted by φ (see Fig. 4), and seven different foliation angles, i.e. $\varphi = 0°, 15°, 30°, 45°, 60°, 75°$ and $90°$, are selected and represented by the numbers from 1 to
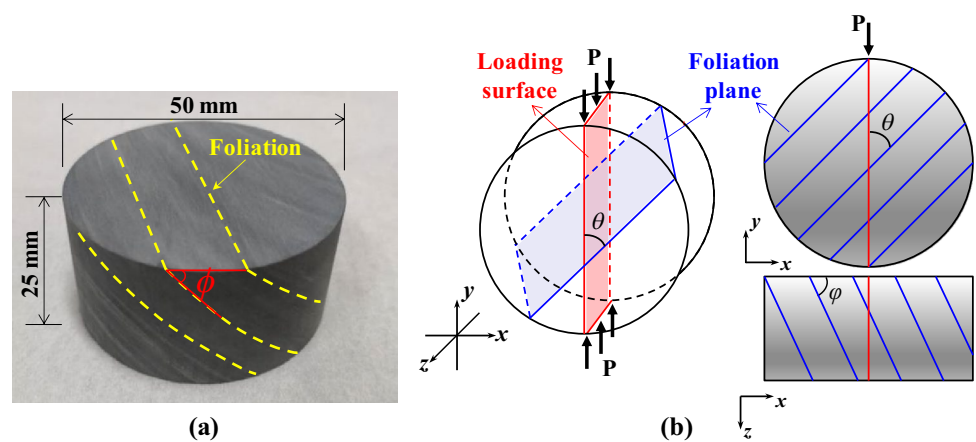
Fig. 2 Site of rock sampling: **a** quarry location, and **b** the outcrop rocks

(a)

(b)
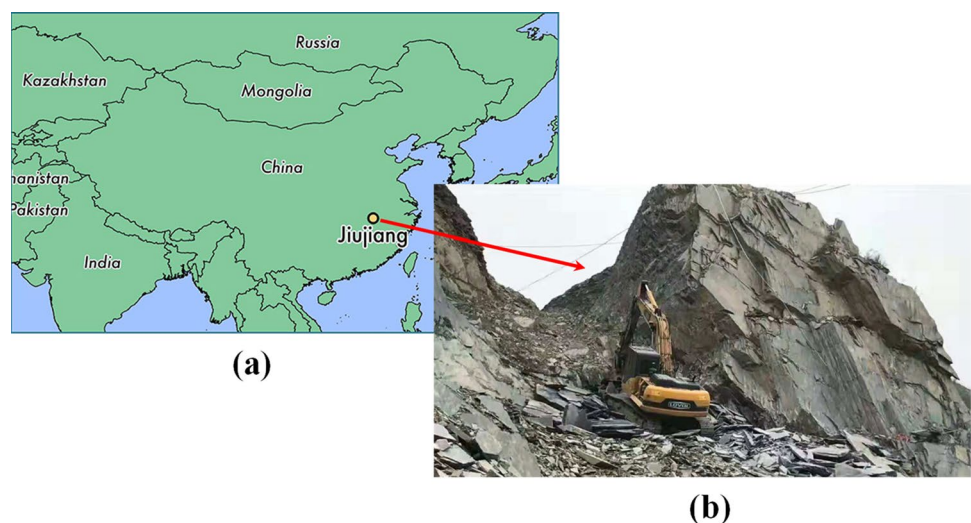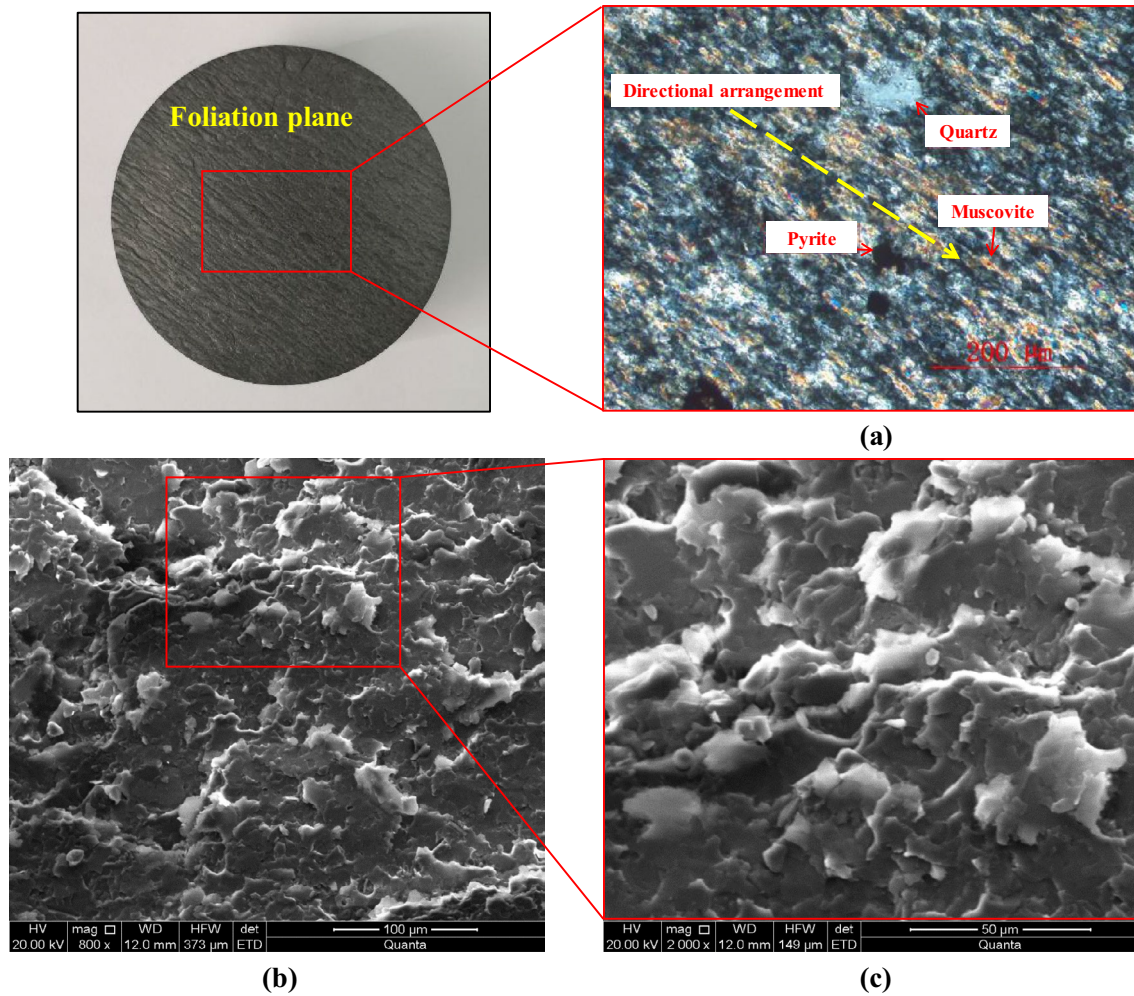
Fig. 3 Microstructure of slate **a** thin section identification ×200 (Ding et al. 2020), **b** SEM image ×800, and **c** SEM image ×2000

Fig. 4 **a** Photo of the drilled disc specimen, and **b** schematic diagram of experimental method (φ and θ represent foliation angle and loading angle, respectively)

7, respectively. The loading angle is defined as the projection of the angle between the loading surface and the foliation plane on the front side of the specimen, as denoted by θ (see Fig. 4b), and five different loading angles, i.e. $\theta = 0°$, 30°, 45°, 60° and 90°, are selected and represented by 0, 30, 45, 60 and 90, respectively. Three repetitive tests (groups A, B and C) are carried out for each combination of foliation angle and loading angle to ensure the accuracy, repeatability, and reliability of the testing results. The numbering method adopted in this paper is named after "Group number–Foliation angle–Loading angle". For example, the specimen C-2–60 means test of group C, foliation angle $\varphi = 15°$, loading angle $\theta = 60°$.

The Brazilian tests were performed using the Rock Mechanics Testing System (RMT150C) with displacement-control method and loading rate of 0.002 mm/s. During the loading process, the AE activity was recorded by the DISP Acoustic Emission Workstation developed by the American Physical Acoustics Corporation. The AE sensor was placed near the centre on the back of the specimen with glue and steel clamps, and vaseline was coated between AE sensor and the specimen, which is conducive to acquisition of the AE signals. The FR-1000 long-time high-speed camera system manufactured by Canadian NORPIX Corporation was used to record the failure process, which was placed in front of the specimen. The arrangements of the testing system are shown in Fig. 5.

3 Test Results

3.1 Applied Failure Force (AFF)

For transversely isotropic rocks (e.g., sandstone, shale, and slate), two main methods are generally applied to calculate the indirect tensile strength in Brazilian tests:

$$\sigma_t = \frac{2P_{max}}{\pi Dt},\tag{1}$$

$$\begin{cases} \sigma_t = \frac{2P_{max}}{\pi Dt}\left[\left(\frac{E}{E'}\right)^{\frac{1}{4}}\cos(2\theta) - \frac{\cos(4\theta)}{4}(b-1)\right] \\ b = \frac{\sqrt{EE'}}{2}\left(\frac{1}{G'} - \frac{2v'}{E'}\right) \end{cases}\tag{2}$$

where σ_t is the indirect tensile strength; P_{max} is the maximum loading force applied to the disc specimen; D and t are the diameter and thickness of the specimen, respectively; θ ranges between 0° and 90°, which denotes the angle between the loading force and foliation plane in 2D space; E and E' are the Young's modulus parallel and perpendicular to the transversely isotropic plane, respectively; G' is the shear modulus perpendicular to transversely isotropic plane; v' is the Poisson's ratio characterising the lateral strain response in the transversely isotropic plane to a stress acting perpendicularly to it.

Two assumptions must be satisfied when using Eq. (1) (ISRM 1978) to calculate the indirect tensile strength, namely (1) the specimens are homogeneous and isotropic, and (2) macro-cracks initiate at the centre of the specimen. To consider the influences of loading direction, Claesson et al. (2002) proposed an explicit analytical solution (see Eq. 2) for calculating the indirect tensile strength of anisotropic rocks. However, there still lacks of suitable method which could consider the both effects of foliation angles and loading angles. In view of the fact that the above calculation methods cannot obtain the accurate indirect tensile strength, for more accurate purpose, the maximum loading force (i.e., applied failure force) recorded by the testing system is used directly to compare the bearing capacity of the specimen that is obtained under Brazilian test conditions. The applied failure force (AFF) of all specimens are tabulated in Table 1 in "Appendix". The average values of each group are plotted in polar coordinate system as shown in Fig. 6.

For the influences of foliation angles, when φ changes from 0° to 90°, the AFF tends to decrease gradually, which

Fig. 5 Experimental set-up: **a** the specimen is placed in loading jaws (central) and monitored both by a high-speed camera (front), and **b** the AE sensor (back)
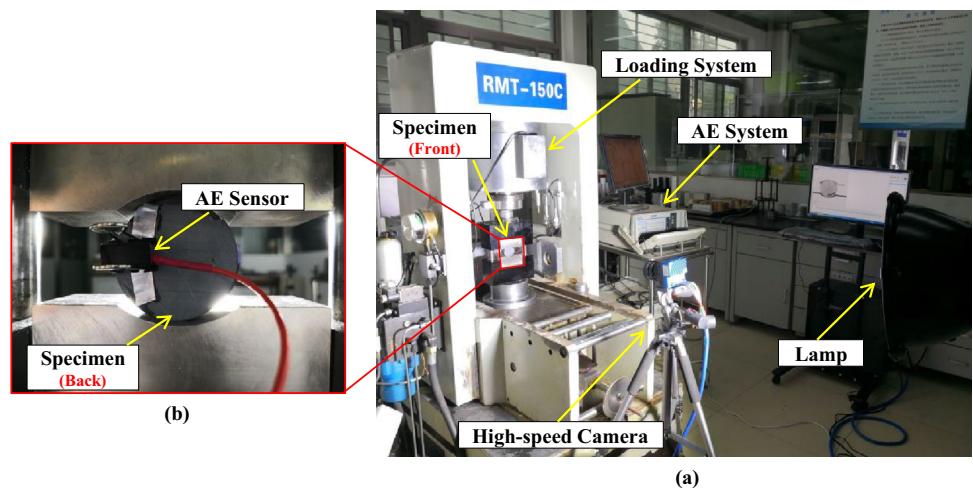
is greatly affected by the loading angles (θ). The variations of AFF with respect to loading angle are significantly different at seven different foliation angles, as illustrated in Fig. 6. In the case of $\varphi = 0°$, the AFF shows small variation with respect to loading angle; when $\varphi = 15°$ and $30°$, the AFF decreases gradually with increase of θ; in the cases of $\varphi = 45°$ and $60°$, the AFF has slight differences, and it first decreases and then increases with increase of θ, with the smallest value at $\theta = 60°$; in the cases of $\varphi = 75°$ and $90°$, the AFF tends to increase gradually, reaching the largest value at $\theta = 90°$, which is consistent with the trend 4 in testing results of Vervoort et al. (2014) as shown in Fig. 1.

For ease comparison, the following normalized AFF′ is used at each foliation angle:

$$\text{AFF}' = \frac{\text{AFF}_\theta}{\text{AFF}_{0°}}, \tag{3}$$

where AFF_θ and $\text{AFF}_{0°}$ are the AFF at the loading angle of θ (e.g., $0°$, $30°$, $45°$, $60°$, and $90°$) and $0°$, respectively. The variations of normalized AFF′ with respect to loading angle at seven different foliation angles are shown in Fig. 7. When $\varphi = 0°$, the normalized AFF′ fluctuates in a small range around 1; in the cases of $\varphi = 15°$–$60°$, the normalized AFF′ is less than 1 and the variation range is relatively small, indicating that the loading angles have a slight influence on AFF; in the cases of $\varphi = 75°$–$90°$, the normalized AFF′ is greater than 1 and the variation range is larger, indicating that the loading angles have a great influence on AFF, showing an obvious increasing trend. The above results indicated that the variations of AFF with respect to loading angle show marked differences at varied foliation angles.

3.2 Fracture Patterns and Mechanisms

According to the typical relationships between the loading force, AE activity, and loading time, it shows that the typical specimen (C-2–60) undergoes five stages, i.e. compaction (stage I), linear elastic deformation (stage II), local-crack initiation and propagation (stage III), macro-crack coalescence (stage IV), and failure (V) during the loading process, as shown in Fig. 8a. At the initial loading stage, the specimen has obvious compaction and AE activity is basically not captured. Once the pre-existing pores and fissures have been compacted, the specimen begins to undergo linear elastic deformation, and AE hits rate shows constant-magnitude AE activities (stage II in Fig. 8a). Prior to this, high-speed camera photos did not provide any useful information. As the loading force continues to increase, AE hits rate first increases significantly due to the fact that a large number of micro-cracks begin to grow, and then the AE energy rate begins to increase with local-crack initiation and propagation. It can be preliminarily concluded that AE hits rate is
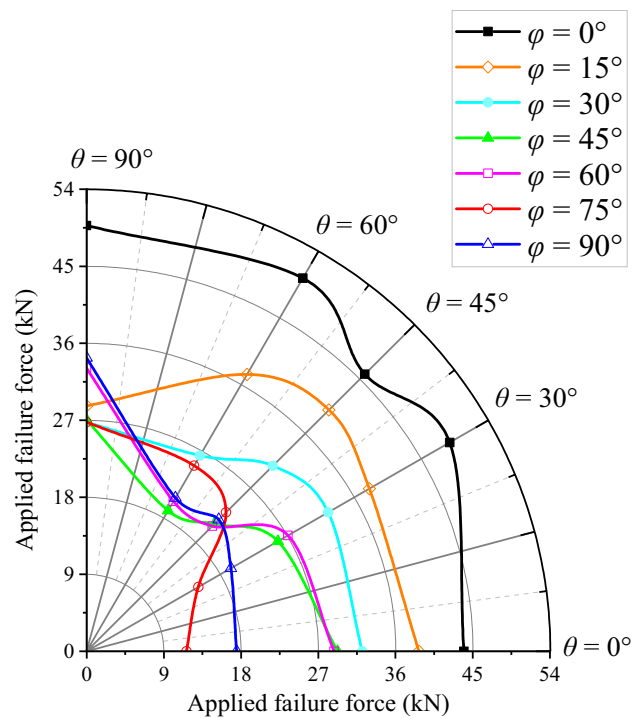

Fig. 6 Average results of AFF with respect to loading angle at different foliation angles
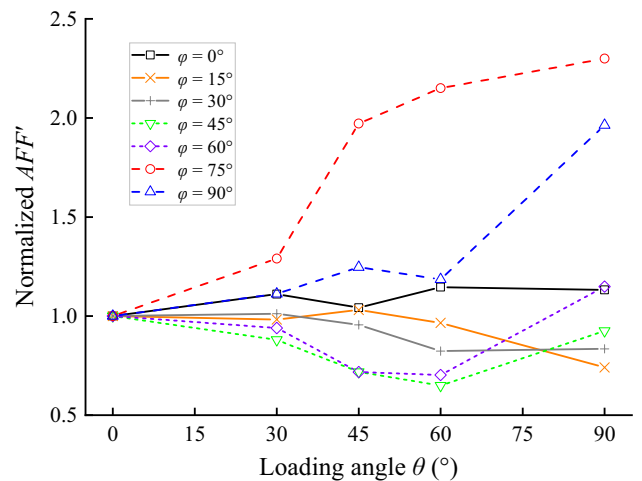

Fig. 7 Variations of normalized AFF′ with loading angle and foliation angle

more sensitive to cracks formation in relatively low stress stage, which is mainly due to the small energy released from the occurrence of micro-cracking (stage III in Fig. 8a). When the loading force reaches 27.77 kN (Point-2), the specimen flank first occurs with local failure to form a macro-crack, which can be clearly observed from photographic monitoring (see Fig. 8b), causing the rate of AE hits and AE energy to increase suddenly. When the loading force reaches

Fig. 8 Monitoring information during the loading process for specimen C-2–60 ($\varphi = 15°$, $\theta = 60°$): **a** the relationships between the loading force, AE activity and loading time, and **b** failure process observed by high-speed camera


(a)

(b)
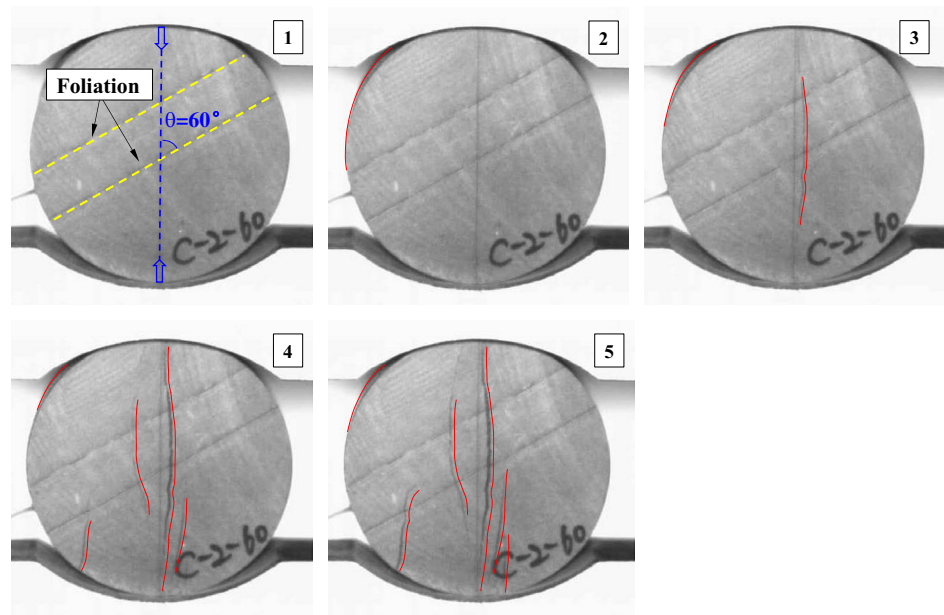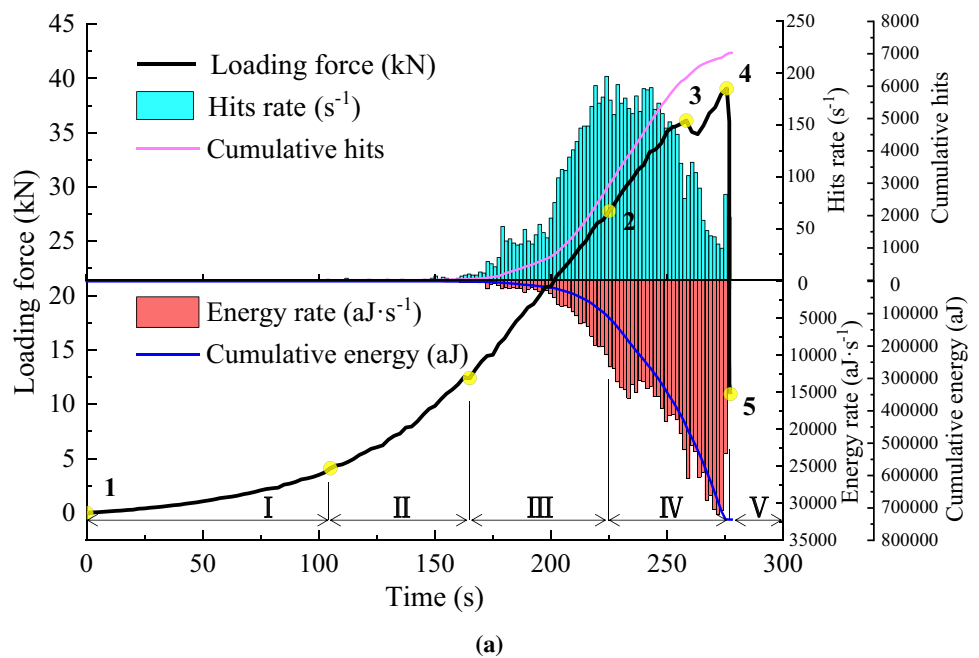
36.11 kN (Point-3), the crack begins to appear on the disc surface, and the stress drops slightly. The AE energy rate increases sharply due to the accumulation of energy inside the specimen released by the macro-cracks coalescence, while the AE hits rate shows a significant drop at this point. This scenario mostly happens during macro-crack coalescence, which mainly due to the overlapping of the hits, as discussed by Moradian et al. (2016). When the loading force reaches the ultimate bearing capacity of 39.06 kN (Point-4), the specimen has strong brittle failure, and the macro-cracks coalesce completely, causing the AE energy rate to

reach the maximum and AE hits rate to show a decreasing trend (stage IV in Fig. 8a), together with a large stress drop (Point-5). In addition, the plots of the cumulative AE hits and AE energy basically show a trend of slow increase and then sharp increase, which are dominated by the local-crack initiation and propagation.

Different from the classical Brazilian tests, we considered the influences of 3D spatial effects of foliation plane in this context. The failure of specimens can be considered as two major processes, namely (1) local failure occurs on the disc flank with a decrease of a small range of loading forces,

Fig. 9 Distribution patterns
of macro-cracks. Red lines
represent the main macro-cracks
(color figure online)

(a) Specimen B-1-1

(b) Specimen A-3-30

(c) Specimen C-5-0

(d) Specimen C-6-30

(e) Specimen B-7-0
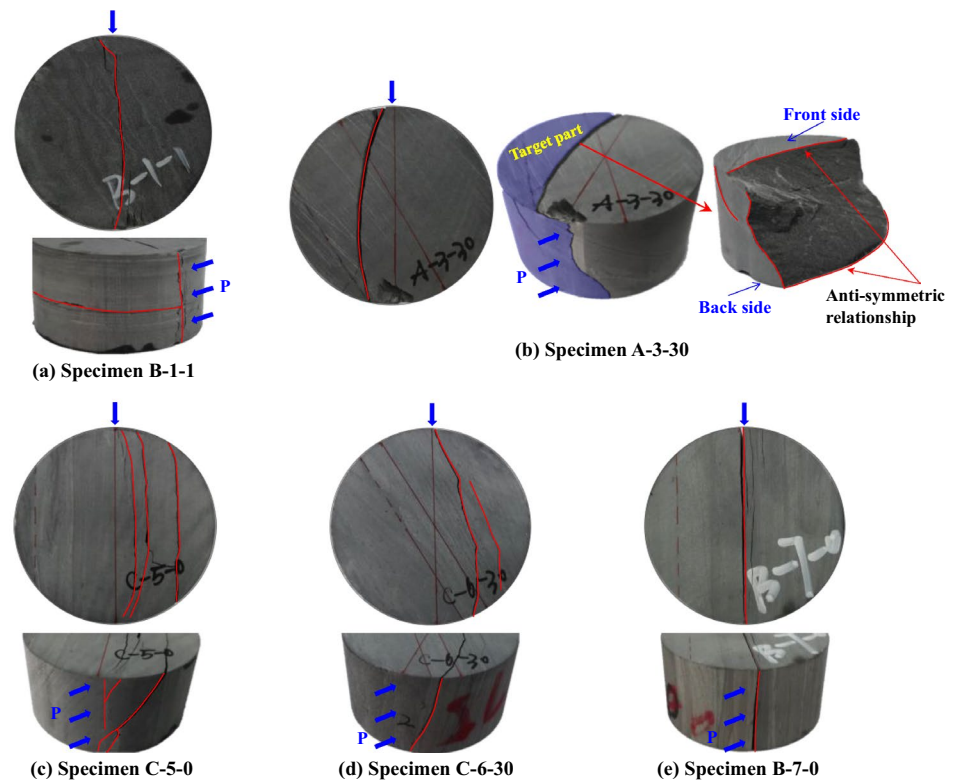
which has a very limited impact on the overall integrity of the rock, and (2) after formation of the fully connected macro-cracks inside the rock, notable brittle failure takes place with dramatically decreasing loading force (Xia et al. 2019). More details about the failure characteristics under the influences of 3D spatial effects of foliation plane will be discussed in the Sect. 3.3.

Tavallali and Vervoort (2010a) also pointed out that the fracture patterns in a few layered sandstone samples are true 3D in the Brazilian tests. However, the 3D spatial effects of fracture patterns in the present work are more complicated with the following characteristics as illustrated in Fig. 9. The fracture patterns on front surface of the typical specimens are displayed in Fig. 10.

1. When the foliation angle is small, i.e. $0° \leq \varphi \leq 15°$, the 3D spatial effects of the fractured surfaces are not sound, and the cracks appearing on the front and back sides of the disc have similarities to some extent. Taking the specimen (B-1-1) as an example (see Fig. 9a), two macro-cracks parallel to the foliation and the loading direction respectively appeared on the disc flank, which were almost perpendicular to each other. A vertical persistent crack appeared on the surface, which belongs to the typical tensile failure. It is noted that the cracks on the surface inflect slightly and deviate from the disc cen-
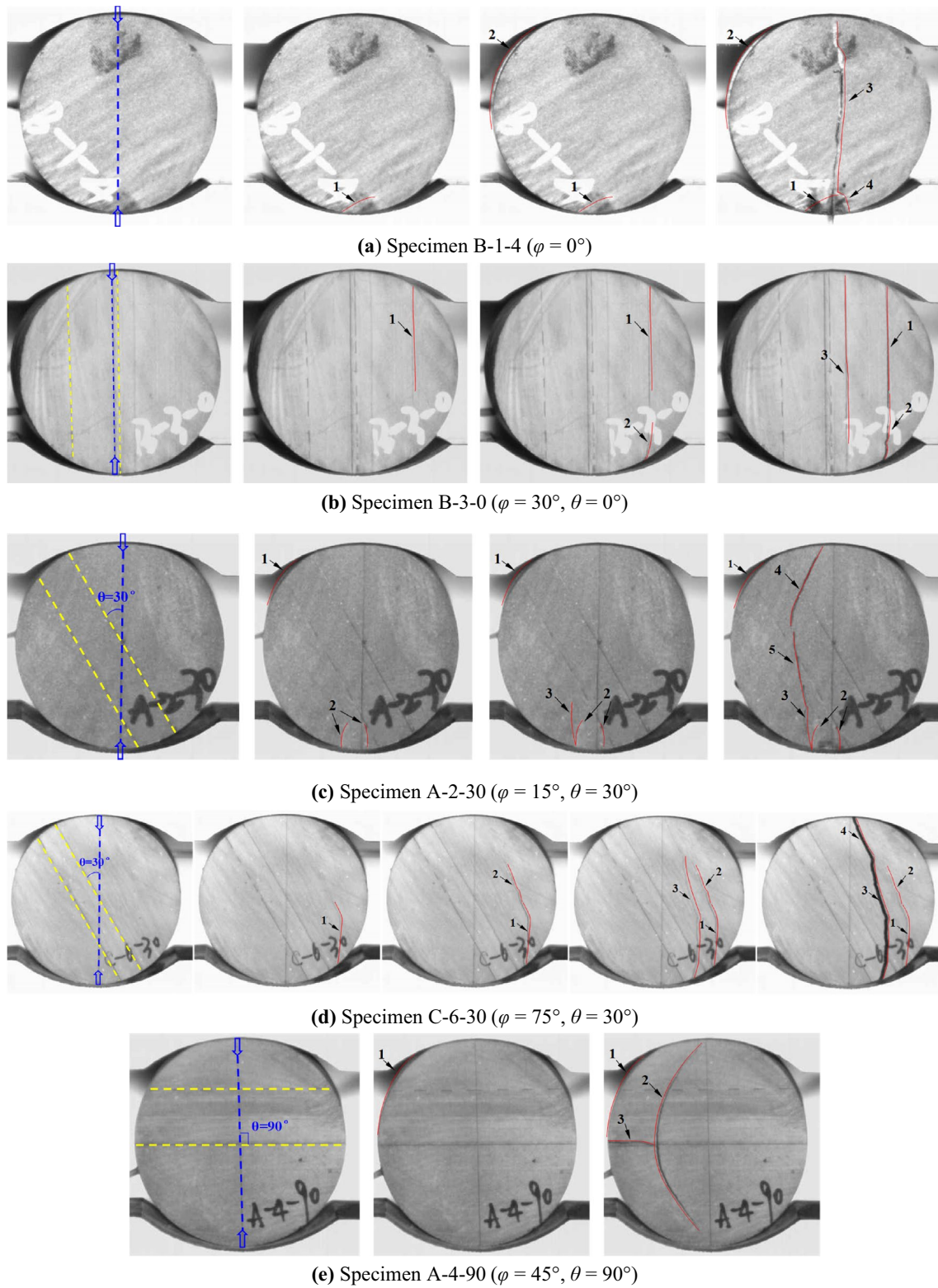
tre under the influences of the foliation angle at $\varphi = 15°$, as shown in Fig. 10.

2. When $\varphi = 30°–60°$, the 3D spatial effects of the fractured surfaces tend to be significant, and the fracture patterns are complicated as certain discreteness of cracking behaviours is observed. The disc flank had one crack mainly parallel to the loading direction and other minor cracks along the foliation, as the number of cracks on the disc flank increases (see Fig. 9b, c). The tensile-shear failure is the major fracture pattern under varied loading angles, as shown in Fig. 10. As mentioned above, the fractured surfaces mainly exhibit 3D spatial distribution, in other words, the macro-cracks on both sides of the specimen are significantly different. Taking the specimen (A-3–30) as an example (see Fig. 9b), the front side was mainly subjected to tensile-shear failure and a circular arc crack appeared. We can target the left part for analysis. It displays that the macro-cracks observed on the front and back sides of the disc present an approximately anti-symmetric relationship. Furthermore, there are local macro-cracks occurring along the foliation on the disc flank, which makes the fractured surface exhibit 3D spatial distribution inside the specimen.

3. When $\varphi = 75°–90°$, the 3D spatial effects of the fractured surfaces are weakened. Taking the specimens (C-6–30 and B-7–0) as examples (see Fig. 9d, e), one macro-crack approximately parallel to the loading direction
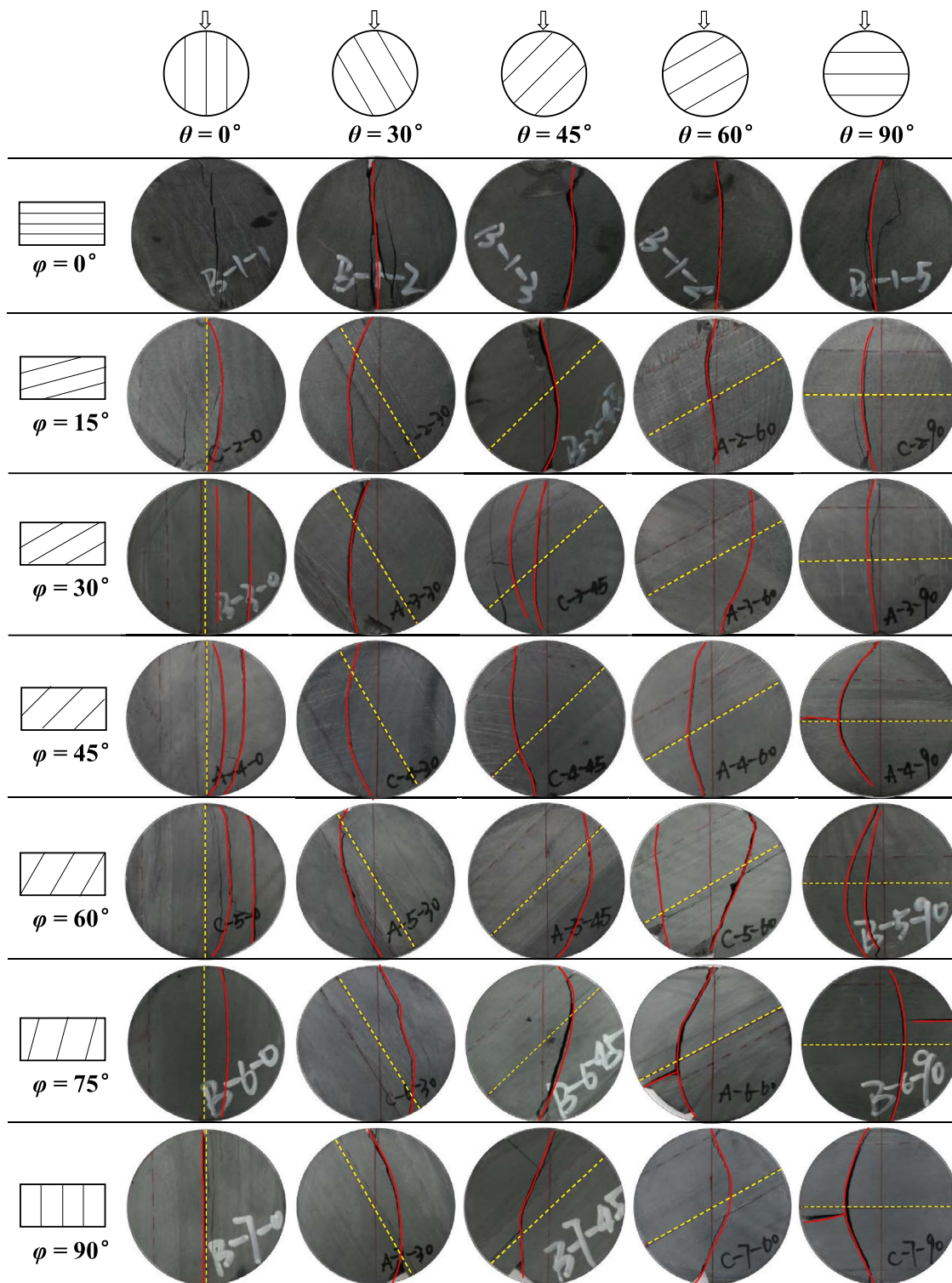
Fig. 10 Fracture patterns of typical specimens under Brazilian test conditions (front surface). Yellow lines and red lines represent the foliation plane and the main macro-cracks, respectively (color figure online)

(a) Specimen B-1-4 ($\varphi = 0°$)

(b) Specimen B-3-0 ($\varphi = 30°$, $\theta = 0°$)

(c) Specimen A-2-30 ($\varphi = 15°$, $\theta = 30°$)

(d) Specimen C-6-30 ($\varphi = 75°$, $\theta = 30°$)

(e) Specimen A-4-90 ($\varphi = 45°$, $\theta = 90°$)

Fig. 11 High-speed photography of failure process for typical specimens. Yellow lines and red lines represent the foliation plane and the cracks, respectively (color figure online)

was mainly formed on the disc flank, and the specimens were of tensile-shear failure and tensile failure, respectively. The fracture patterns are highly similar on both sides, which can be considered as 2D in this case. In addition, the fracture patterns show a certain sensitivity to the loading direction, i.e. tensile failure along the foliation ($\theta = 0°$), tensile-shear failure ($\theta = 30°$–$60°$), and tensile failure across the foliation ($\theta = 90°$), as observed in Fig. 10. This phenomenon is in good agreement with the results observed in the Brazilian tests of other anisotropic rocks in previous studies (e.g., Vervoort et al. 2014; Wang et al. 2016; Zhang et al. 2018). Hence, the Brazilian tests for traditional anisotropic rocks (i.e., considering 2D case) are perhaps a special case of this work.

3.3 Failure Process Analysis

In this study, the failure process was recorded by a high-speed camera with a speed of 1000 frames per second, and its advantages lie in long-time shooting, which can record the whole rock failure process. The specific failure process for typical specimens is analysed herein.

Taking the specimen B-1–4 ($\varphi = 0°$) as an example, micro-cracks first appeared near the lower loading position due to the stress concentration (e.g. crack 1), then the splitting failure occurred along the foliation on the disc flank (e.g. crack 2). Finally, a subvertical crack initiated at lower loading position and propagated upward along the loading direction (e.g. crack 3), as shown in Fig. 11a. In this case, the failure type can be considered as the pure tensile failure across the rock matrix, similar to the failure type of isotropic material under Brazilian test conditions (Basu et al. 2013; Dan et al. 2013).

When $\theta = 0°$ (i.e., the loading direction is parallel to the foliation), the crack in specimen B-3–0 ($\varphi = 30°$) initiated at the disc flank and propagated to the front surface to form a macro-crack along the foliation (e.g., cracks 1, 2). With increase of loading force, a vertical persistent crack was observed near the centreline, causing the overall failure of the specimen (e.g., crack 3), as shown in Fig. 11b. When $\theta = 30°$, the crack in specimen A-2–30 ($\varphi = 15°$) first appeared on the disc flank (e.g., crack 1), and then the cracks started at the upper and lower loading positions and propagated across the foliation to the disc centre (e.g., cracks 2–5), forming a circular arc crack on the front surface under the tensile and shear stresses, as shown in Fig. 11c. As for the specimen C-6–30 ($\varphi = 75°$), the crack initiated from the boundary of the disc surface and propagated along the

loading direction, after which it propagated along the foliation (e.g., cracks 1, 2). At the same time, another new crack was observed near the disc centre, and it coalesced rapidly due to the close distance to the loading points (e.g., cracks 3, 4), as shown in Fig. 11d. When $\theta = 90°$ (i.e., the loading direction is perpendicular to the foliation), the crack in specimen A-4–90 ($\varphi = 45°$) first appeared on the disc flank (e.g., crack 1), and then a circular arc crack across the foliation which deviated from the disc centre was observed on the front surface (e.g., crack 2). In addition, the secondary crack along the foliation appeared at the boundary and it propagated towards the disc centre (e.g., crack 3), as shown in Fig. 11e.

The failure process recorded by the high-speed camera was varying significantly with different foliation and loading angles. At lower foliation angles, the local failure on the disc flank was obvious, and the overall failure was likely to be induced by the macro-cracks coalesced inside the specimen (see Fig. 11a–c, e). By contrast, there is no obvious local failure on the disc flank at larger foliation angles, and the fracture pattern can be considered as 2D consequently (see Fig. 11d). The common point is that the main cracks observed from the disc surface are generally initiated at the loading positions under the influences of foliation plane or stress concentration, and then they propagate and coalesce along or across foliation to the centre or boundaries of the disc, which is consistent with the experimental observations of Xu et al. (2018). The final fracture patterns are significantly different due to the varied combinations of foliation angle and loading angle, as discussed in Sect. 3.2. It can also be seen from the failure process of typical specimens that the loading angles play a decisive role in the fracture patterns, while the foliation angles are the main cause of the local failure on the disc flank. The local failure affects the distribution of the fractured surface inside the specimen to some extent, so that it shows the characteristics of 3D spatial distribution, as illustrated in Fig. 9b.

3.4 AE Distribution Characteristics

The high-speed camera visually recorded the crack initiation, propagation and coalescence from the outside of the specimen. When micro-fracture and crack propagation occur inside the rock during the loading process, the strain energy will be released in a form of elastic waves, i.e. acoustic emission (AE). AE is widely used to detect cracks growth regarding the failure process in rock (Lockner 1993; Moradian et al. 2016). Thus, the AE hits and AE energy are used to analyse the rupture evolution inside the specimen, as they
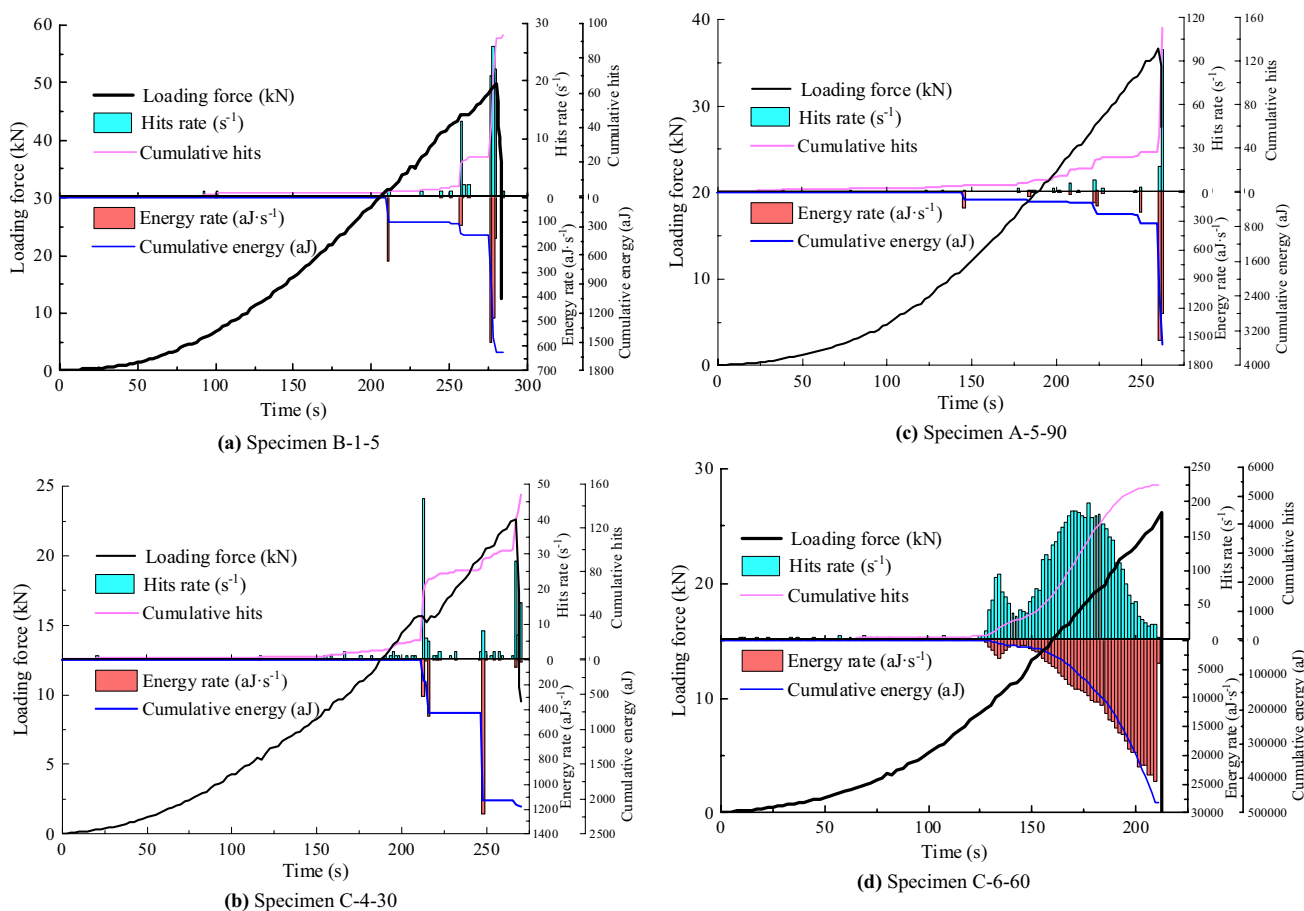
(a) Specimen B-1-5

(c) Specimen A-5-90

(b) Specimen C-4-30

(d) Specimen C-6-60

Fig. 12 Temporal distributions of AE activity for typical specimens

are closely related to the number of growing cracks and magnitude of cracking events, respectively (Moradian et al. 2016). Figure 12 displays the temporal distributions of AE activity for the typical specimens. The AE energy can be derived from the integral of squared voltage divided by the internal resistance as follows:

$$E = \frac{1}{R} \int_{t_i}^{t_j} U^2(t)\mathrm{d}t, \tag{4}$$

where t_i and t_j are the start and end times of the AE activity; R is the internal resistance; the duration of the AE activity is $\Delta t = t_j - t_i$.

When the foliation angle is small (e.g., $\varphi = 0°$ or $15°$), taking the specimen (B-1–5) as an example (see Fig. 12a), there is fewer AE activity at the initial loading stage, and the AE energy and AE hits suddenly increase due to the occurrence of local-cracks. As the macro-cracks coalesce inside the specimen, the AE activity increases again. Thus, the

plots of the cumulative AE hits and AE energy present the "stepped" increasing mode, specifically "double-stepped", which is related to the two main processes of local and overall failures, as discussed in Sect. 3.2. The relatively weak AE activity caused by local failure indicates that the local failure has slight effects on decreasing the overall integrity of the specimen.

When the foliation angle φ is between $30°$ and $60°$, taking the specimens (C-4–30 and A-5–90) as examples (see Fig. 12b, c), the AE activity is stronger compared with that of low foliation angle (i.e., $\varphi = 0°$ or $15°$), indicating that the continual propagation of cracks occurs inside the specimen under this testing condition. The plots of the cumulative AE energy and AE hits mainly exhibit "multi-stepped" increasing mode, which reflects the characteristics of "progressive failure", including the local and overall failures. The propagation path of the cracks is more complicated, as the fractured surface is with a 3D spatial distribution. The difference is that when $\theta = 30°$ (specimen C-4–30 in Fig. 12b), the AE
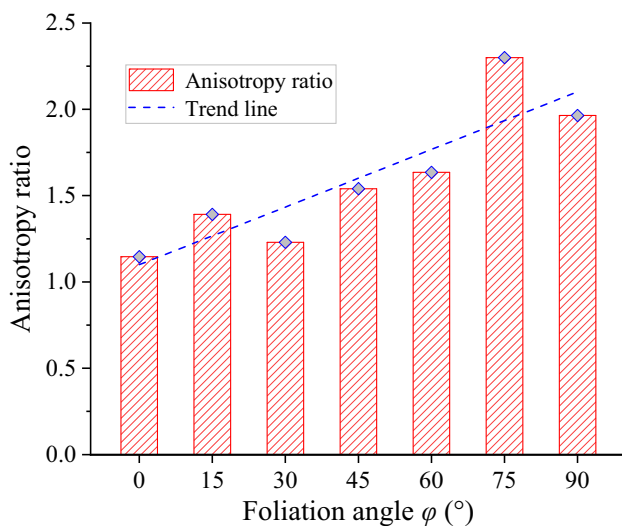
Fig. 13 The relationship between anisotropy ratio and foliation angle

activity induced by local failure is more intense, while the AE activity is more uniform at $\theta = 90°$ (specimen A-5–90 in Fig. 12c).

When the foliation angle is large (e.g., $\varphi = 75°$ or $90°$), taking the specimen (C-6–60) as an example (see Fig. 12d), AE hits rate is denser at the beginning of loading due to its higher sensitivity to cracks formation, as mentioned in Sect. 3.2, while the AE energy rate is weak. When the loading is about 50% of the ultimate bearing capacity of the specimen, a significant growth of AE activity is recorded. When approaching the peak, the AE energy increases gradually, while the AE hits show a decreasing trend due to the overlapping of the hits (Moradian et al. 2016). The plots of the cumulative AE energy and AE hits have a "flat-to-continuously" increasing mode. Nevertheless, the "stepped" increasing mode of the cumulative AE activity disappears in this case, and the specimen failure can then be considered as 2D. In this case, the overall failure is apparent, forming the similar cracks on the front and back sides.

Interestingly, the AE hits rate of some specimens show a decreasing trend in the macro-crack coalescence stage, which results in the plots of the cumulative AE hits inclining to zero, as observed in Fig. 12a, d. This is mainly due to the high cracking rate, that is, when two cracks appear simultaneously, the second hit due to the second crack development exceeds the threshold value while the first hit is still being measured, which causes overlapping of the hits (Moradian et al. 2016). Although the obtained results have a certain similarity in terms of cumulative AE hits near the peak, the rock failure mechanisms are very different from each other. The specimen B-1–5 was subjected to tensile failure, while the specimen C-6–60 was mainly controlled by tensile-shear failure, but the fractured surfaces of both present 2D spatial

distribution, as discussed in Sect. 3.2. This can reflect a simple crack propagation path compared to the cases of $\varphi = 30°–60°$ and explain the high cracking rate at the high-stress level, thus the cumulative AE hits show the similar characteristics near the peak (see Fig. 12a, d). This phenomenon can also be found in the specimen C-2–60, as shown in Fig. 8a. In contrast, this does not appear in the plots of the cumulative AE hits for the specimens at $\varphi = 30°–60°$, due to the relatively complicated cracking path reflected by the 3D spatial effects of the fractured surfaces. The plots of the cumulative AE hits show a gradually "stepped" increasing until the peak, indicating the continual increase in the number of macro-cracks. This also explains the characteristics of "progressive failure". The above analyses of AE activity can better facilitate our understanding of the rock failure characteristics in 3D space under Brazilian test conditions.

4 Discussion

4.1 Anisotropy Ratio of AFF

According to the anisotropy ratio proposed by Cho et al. (2012), anisotropy ratio of AFF can be calculated as follows:

$$\alpha(\varphi) = \frac{\text{AFF(max)}}{\text{AFF(min)}}, \qquad (5)$$

where $\alpha(\varphi)$ is the anisotropy ratio of AFF, AFF(max) and AFF(min) are the maximum and minimum values related to the loading angles at each foliation angle, respectively. The calculation results are shown in Fig. 13, indicating obvious anisotropies in AFF. As the foliation angle increases, the anisotropy ratio values show an increasing trend, that is, more significant anisotropy can be noted. In this sense, the foliation angles have a crucial influence on the anisotropies of slate. In the Brazilian tests of transversely isotropic rocks, the 3D spatial effects of foliation plane determined by the foliation and the loading angles should be taken into account.

4.2 Foliation Effects of Slate in 3D Space

Both foliation and loading angles have significant impacts on AFF, failure process, and fracture patterns, which can be seen from the typical force–time curve and the rupture evolution process (i.e., AE activity and high-speed photography), as illustrated in Fig. 8. During the loading process, local failure first occurred on the disc flank with macro-cracks, resulting in decline of a small range of loading force. When the foliation angle is small, the local failure has slight influences on the bearing capacity of the specimen. As the foliation angle increases, the local failure changes from

Fig. 14 Variations of CFE with foliation angle and loading angle
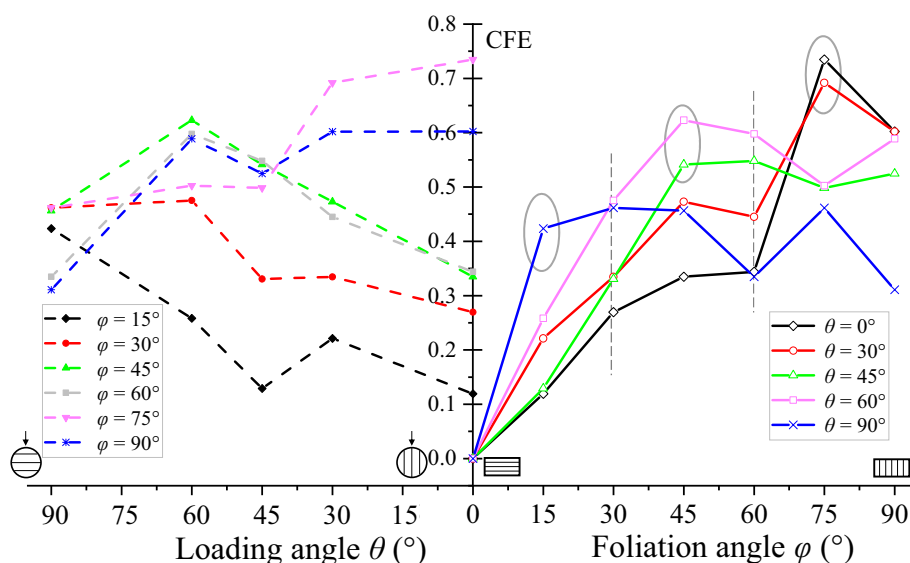
splitting to shearing. There is a certain angle between the local-cracks on the flank and the disc surface, which can accelerate crack propagation and coalescence inside the specimen, causing the overall failure. This can significantly weaken the mechanical properties of slate, and the weakening effects become more obvious with increase of foliation angle. In other words, the foliation angle determines the influences of local failure on the bearing capacity. Therefore, the AFF tends to decrease with increase of foliation angle, as shown in Fig. 6.

Xu et al. (2018) pointed out that the failure strengths are closely related to the fracture patterns when conducting the Brazilian tests of layered phyllite. In view of fracture patterns, when $\theta = 0°$ (i.e., loading direction is parallel to the foliation), the tensile failure along the foliation planes appears. Due to the small cohesion between the foliation planes, the AFF is lower in this case. When $\theta = 90°$ (i.e., the loading direction is perpendicular to the foliation), the tensile failure across the foliation planes occurs. Due to the high bearing capacity of the slate matrix, the AFF is higher subsequently. When the loading direction is oblique to the foliation (say $\theta = 30°$–$60°$), the tensile-shear failure across foliation planes can be observed, and the AFF is in between the cases of $\theta = 0°$ and $90°$. Pure shear failure along the foliation may also occur locally, resulting in lower strength. Many researchers have drawn the similar conclusions based on 2D case (e.g., Debecker and Vervoort 2009; Vervoort et al. 2014; Mokhtari and Tutuncu 2016; Wang et al. 2018). However, when considering the coupling of the foliation and loading angles, the variation trends of AFF with respect to loading angle are not always the same under the influences of foliation angles, as discussed in Sect. 3.1. Hence, it is likely that the coupling of foliation and loading angles has a crucial influence on the mechanical and

failure characteristics of slate in the Brazilian tests. This is the reason that it is rather difficult to reach a consensus on the variation of indirect tensile strength of transversely isotropic rocks with respect to loading direction, that is, the 3D spatial effects of the bedding or foliation plane.

Among all the testing results (see "Appendix"), the AFF reaches the maximum value at $\varphi = 0°$ and is independent of the loading angles. With increase of foliation angle, the AFF tends to decrease, and it is significantly affected by the loading angles. To intuitively illustrate the influences of foliation and loading angles on the results of the Brazilian tests, the coefficient of foliation effects (CFE) is introduced as a function of φ and θ for analysis. The calculation method is as follows:

$$\text{CFE} = 1 - \frac{\text{AFF}(\varphi)}{\text{AFF}(0°)}, \tag{6}$$

where $\text{AFF}(\varphi)$ and $\text{AFF}(0°)$ are the AFF at the foliation angle of φ and $0°$, respectively.

Figure 14 displays the calculation results, and the left and right parts respectively show the variations of CFE as a function of loading angle and foliation angle. The CFE reflects the weakening degree of the AFF with different foliation angles relative to $\varphi = 0°$, the larger the CFE, the more significant the weakening degree of AFF. As can be seen from the right part in Fig. 14, under different loading angles, the CFE curves generally show an increasing trend with increase φ. When the foliation angle is small (e.g., $\varphi = 0°$–$30°$), the CFE is the largest at $\theta = 90°$. When $\varphi = 30°$–$60°$, the CFEs are larger at $\theta = 45°$ and $60°$. When the foliation angle is comparatively large (e.g., $\varphi = 60°$–$90°$), the CFEs are larger at $\theta = 0°$ and $30°$. It can also be noticed that the influences of foliation angles on the testing results vary with the loading

angles. On the other hand, it can be seen from the left part in Fig. 14 that the CFE curves show the trends of gradual increasing ($\varphi = 15°$–$30°$), increasing first and then decreasing ($\varphi = 45°$–$60°$), and gradual decreasing ($\varphi = 75°$–$90°$) with respect to loading angle. That is to say, the effects of foliation angle are significant at $\varphi = 45°$–$60°$, which is in good agreement with the analyses of the failure characteristics, i.e. the 3D spatial distribution of the fractured surface in this context. The above analyses indicated that the variations in foliation angle have led to the diversity of fracture patterns, which has affected the bearing capacity of the rock to some extent. Therefore, the bedding or foliation angles of transversely isotropic rocks should be considered as an important indicator in the Brazilian tests, to avoid adverse effects on the testing results and actual engineering design.

For failure characteristics, when the foliation angle is small (e.g., $\varphi = 0°$–$15°$), both the local splitting failure on the flank and the overall failure of the specimen are more severe, which belongs to the typical tensile failure behaviour. Both of the two major processes cause the AE activity to increase suddenly and as a result, the plots of the cumulative AE activity show "double-stepped" increasing mode. When $\varphi = 30°$–$60°$, the characteristics of "progressive failure" are remarkable, which are manifested in the tensile-shear failure behaviour. The local shearing failure is dominant on the flank, which has a great influence in decreasing the overall integrity of the rock. The AE activity is denser, the plots of the cumulative AE energy and AE hits are mainly characterised by "multi-stepped" growth. In this sense, the fractured surfaces mainly exhibit evident 3D spatial distribution, and the macro-cracks on both sides of the specimen present an approximately anti-symmetric relationship. The main reason accounting for this scenario is that the specimen failure is considered as two processes. Local failure occurs on the disc flank, and the cracks generated by the local failure provide the preferable direction for rock failure. The cracks propagate and coalesce from the cracks tip to form macro-cracks, resulting in the overall failure of the specimen. The superposition of the two major failure processes suggests that the fractured surfaces have 3D spatial distribution characteristics inside the specimen. This means a wide distribution of macro-cracks, forming the complex fracture network with good connectivity. When the foliation angle is large (e.g., $\varphi = 75°$–$90°$), the loading angles have a great influence on failure process. The fracture patterns are mainly divided into tensile failure along the foliation ($\theta = 0°$), tensile-shear failure ($\theta = 30°$–$60°$), and tensile failure across the foliation ($\theta = 90°$), which can be considered as 2D due to the similarity of macro-cracks to some extent on both sides. The AE activity began to gradually increase until loading to 50% of the ultimate bearing capacity, and the plots of the cumulative AE activity are of "flat-to-continuously" increasing mode.

According to the results of the high-speed photography, although the local failure is more evident when φ is in the range of $0°$–$60°$, the main reason for the overall failure is that the macro-cracks are completely connected inside the specimen. The cracks generally initiate at the loading positions, and finally propagate and coalesce along or across foliation to the centre or boundaries of the disc.

It is conclusive that the accurate evaluation of tensile mechanical properties of the rock in 3D space under Brazilian test conditions is an important research topic. The new findings of this work may be of great significance for hydraulic fracturing of hydrocarbon exploitation with layered structures (Barton and Quadros 2015; Mokhtari and Tutuncu 2016; Yang et al. 2019; Zuo et al. 2020). The tensile strength determines the hydraulic fracture initiation, thus fracturing pressure is high at $\varphi = 0°$ and gradually decreases with increase of φ, and the fracture patterns can reflect the geometry of the fracture network to some extent. Qualitatively speaking, more complex fracture network may be obtained under relatively low fracturing pressure near $\varphi = 45°$.

5 Conclusions

The Brazilian tests of slate with foliation structures were performed in this context, taking into account foliation and loading angles, i.e. 3D spatial effects of foliation plane. The AFF, failure characteristics and rupture evolution process of slate were analysed and discussed. The main conclusions are drawn as follows:

1. Both foliation angles and loading angles have a crucial influence on the bearing capacity of slate. The AFF decreases gradually as the foliation angle φ changes from $0°$ to $90°$. Due to the combined effects of the two factors, the variations of AFF with respect to loading angle are not always the same under seven different foliation angles. The anisotropy ratio of AFF shows an increasing trend with increase of φ, and suggesting more significant rock anisotropy.

2. When the foliation angle is small, i.e. $0° \leq \varphi \leq 15°$, or large, i.e. $75° \leq \varphi \leq 90°$, the fracture patterns can be considered as 2D due to the similarity of macro-cracks to some certain on both sides (i.e., front and back) of the specimen. When φ is in the range of $30°$–$60°$, the fractured surfaces exhibit 3D spatial distribution inside the specimen, thus the macro-cracks observed on the both sides of the disc present an approximately anti-symmetric relationship, forming the complex fracture with good connectivity in this case.

3. The specimen failure can be regarded as two major processes with a combined analyses of AE activity and photographic monitoring. Local failure first occurs on the disc flank, and then the fully connected cracks are formed causing the overall failure. It should be noted that the second process dominates the bearing capacity of the rock to a greater extent. Good agreements are observed between the high-speed photography and AE activity in terms of failure process, and AE hits and AE energy are utilized to distinguishing the local- and macro-cracks.

4. New insights are proposed for the indirect tensile behaviour of anisotropic rocks, i.e. the 3D spatial effects of foliation plane, which should be considered due to its important influences on the mechanical and failure characteristics. The preliminary findings reported in this context may have inspirations for the practical projects with layered strata, such as hydraulic fracturing and underground excavation.

Compliance with Ethical Standards

Conflict of interest The authors declare that there is no conflict of interest in the present study.

Appendix

See Table 1.

Table 1 Brazilian tests results of all the slate specimens

Foliation angle	Applied failure force (kN)					
	Group	$\theta=0°$	$\theta=30°$	$\theta=45°$	$\theta=60°$	$\theta=90°$
$\varphi=0°$	B	43.94	48.81	45.80	50.36	49.76
$\varphi=15°$	A	41.85	39.08	40.77	35.28	30.25
	B	35.91	38.41	39.62	37.73	25.92
	C	38.32	36.55	39.29	39.06	29.86
Average		38.69	38.01	39.89	37.36	28.68
$\varphi=30°$	A	35.03	33.71	31.81	29.07	27.42
	B	30.53	30.95	28.35	23.13	27.05
	C	30.72	32.78	31.82	27.05	25.86
Average		32.09	32.48	30.66	26.42	26.78
$\varphi=45°$	A	28.20	28.04	25.65	24.42	31.01
	B	29.65	26.48	21.10	19.37	27.53
	C	29.84	22.65	16.27	13.15	22.60
Average		29.23	25.72	21.01	18.98	27.05
$\varphi=60°$	A	29.11	25.83	25.85	21.25	28.28
	B	26.24	26.98	19.48	20.71	36.70
	C	31.12	28.44	16.75	18.79	34.32
Average		28.82	27.08	20.69	20.25	33.10
$\varphi=75°$	A	13.90	12.91	23.76	22.91	28.62
	B	10.07	17.01	26.58	26.11	24.70
	C	10.98	15.16	18.56	26.13	27.04
Average		11.65	15.03	22.97	25.05	26.79
$\varphi=90°$	A	14.37	13.73	24.97	16.67	39.32
	B	18.68	24.98	19.79	20.80	31.78
	C	19.35	19.56	20.56	24.64	31.79
Average		17.47	19.42	21.77	20.70	34.30

References

Al-Bazali TM, Zhang JG, Chenevert ME, Sharma MM (2005) Measurement of the sealing capacity of shale caprocks. In: SPE annual technical conference and exhibition, Dallas, Texas. https://doi.org/10.2118/96100-MS

Amann F, Kaiser P, Button EA (2012) Experimental study of brittle behavior of clay shale in rapid triaxial compression. Rock Mech Rock Eng 45(1):21–33. https://doi.org/10.1007/s00603-011-0195-9

Barla G (1974) Rock anisotropy: theory and laboratory testing. Rock Mech 131–169

Barton N, Quadros E (2015) Anisotropy is everywhere, to see, to measure, and to model. Rock Mech Rock Eng 48(4):1323–1339. https://doi.org/10.1007/s00603-014-0632-7

Basu A, Mishra DA, Roychowdhury K (2013) Rock failure modes under uniaxial compression, Brazilian, and point load tests. Bull Eng Geol Environ 72:457–475. https://doi.org/10.1007/s10064-013-0505-4

Bohloli B, Ronge B, Gustafson G (2002) Laboratory examination of anisotropy in the foliation plane of metamorphic rocks. Bull Eng Geol Environ 61:43–47. https://doi.org/10.1007/s100640100110

Cai M, Kaiser PK (2004) Numerical simulation of the Brazilian test and the tensile strength of anisotropic rocks and rocks with preexisting cracks. Int J Rock Mech Min Sci 41(3):450–451. https://doi.org/10.1016/j.ijrmms.2003.12.111

Carneiro F, Barcellos A (1953) International association of testing and research laboratories for materials and structures. RILEM Bull 13:99–125

Chen CS, Pan E, Amadei B (1998) Determination of deformability and tensile strength of anisotropic rock using Brazilian tests. Int J Rock Mech Min Sci 35(1):43–61. https://doi.org/10.1016/S0148-9062(97)00329-X

Cho JW, Kim H, Jeon S, Min KB (2012) Deformation and strength anisotropy of Asan gneiss, Boryeong shale, and Yeoncheon schist. Int J Rock Mech Min Sci 50:158–169. https://doi.org/10.1016/j.ijrmms.2011.12.004

Claesson J, Bohloli B (2002) Brazilian test: stress field and tensile strength of anisotropic rocks using an analytical solution. Int J Rock Mech Min Sci 39(8):991–1004. https://doi.org/10.1016/S1365-1609(02)00099-0

Dan DQ, Konietzky H, Herbst M (2013) Brazilian tensile strength tests on some anisotropic rocks. Int J Rock Mech Min Sci 58:1–7. https://doi.org/10.1016/j.ijrmms.2012.08.010

Debecker B, Vervoort A (2009) Experimental observation of fracture patterns in layered slate. Int J Fract 159(1):51–62. https://doi.org/10.1007/s10704-009-9382-z

Delle Piane C, Almqvist BSG, Macrae CM, Torpy A, Mory AJ, Dewhurst DN (2015) Texture and diagenesis of Ordovician shale from the Canning Basin, Western Australia: implications for elastic anisotropy and geomechanical properties. Mar Pet Geol 59:56–71. https://doi.org/10.1016/j.marpetgeo.2014.07.017

Ding CD, Hu DW, Zhou H, Lu JJ, Lv T (2020) Investigations of P-wave velocity, mechanical behavior and thermal properties of anisotropic slate. Int J Rock Mech Min Sci 127:104176. https://doi.org/10.1016/j.ijrmms.2019.104176

Duan K, Kwok CY (2015) Discrete element modeling of anisotropic rock under Brazilian test conditions. Int J Rock Mech Min Sci 78:46–56. https://doi.org/10.1016/j.ijrmms.2015.04.023

Everitt RA, Lajtai EZ (2004) The influence of rock fabric on excavation damage in the Lac du Bonnet granite. Int J Rock Mech Min Sci 41(8):1277–1303. https://doi.org/10.1016/j.ijrmms.2004.09.013

Garcia-Fernandez CC, Gonzalez-Nicieza C, Alvarez-Fernandez MI, Gutierrez-Moizant RA (2019) New methodology for estimating the shear strength of layering in slate by using the Brazilian test.

Bull Eng Geol Environ 78:2283–2297. https://doi.org/10.1007/s10064-018-1297-3

Gholami R, Rasouli V (2014) Mechanical and elastic properties of transversely isotropic slate. Rock Mech Rock Eng 47(5):1763–1773. https://doi.org/10.1007/s00603-013-0488-2

Ho NC, van der Pluijm BA, Peacor DR (2001) Static recrystallization and preferred orientation of phyllosilicates: Michigamme Formation, Northern Michigan, USA. J Struct Geol 23(6):887–893. https://doi.org/10.1016/S0191-8141(00)00162-0

Hu DW, Zhou H, Zhang F, Shao JF, Zhang JF (2013) Modeling of inherent anisotropic behavior of partially saturated clayey rocks. Comput Geotech 48:29–40. https://doi.org/10.1016/j.compgeo.2012.09.002

Hu SC, Tan YL, Zhou H, Guo WY, Hu DW, Meng FZ, Liu ZG (2017) Impact of bedding planes on mechanical properties of sandstone. Rock Mech Rock Eng 50(8):2243–2251. https://doi.org/10.1007/s00603-017-1239-6

ISRM (1978) Suggested methods for determining tensile strength of rock materials. Int J Rock Mech Min Sci Geomech Abstr 15(3):99–103. https://doi.org/10.1016/0148-9062(78)90003-7

Jaeger JC, Cook NGW, Zimmerman R (2009) Fundamentals of rock mechanics. Wiley, New York

Kim H, Cho JW, Song I, Min KB (2012) Anisotropy of elastic moduli, P-wave velocities, and thermal conductivities of Asan Gneiss, Boryeong Shale, and Yeoncheon Schist in Korea. Eng Geol 147–148:68–77. https://doi.org/10.1016/j.enggeo.2012.07.015

Li DY, Wong LNY (2013) The Brazilian disc test for rock mechanics applications: review and new insights. Rock Mech Rock Eng 46(2):269–287. https://doi.org/10.1007/s00603-012-0257-7

Lisjak A, Tatone BSA, Mahabadi OK et al (2016) Hybrid finite-discrete element simulation of the EDZ formation and mechanical sealing process around a microtunnel in Opalinus Clay. Rock Mech Rock Eng 49(5):1849–1873. https://doi.org/10.1007/s00603-015-0847-2

Liu ZJ, Zhang CQ, Zhang CS, Gao Y, Zhou H, Chang ZR (2019) Deformation and failure characteristics and fracture evolution of cryptocrystalline basalt. J Rock Mech Geotech Eng 11(5):990–1003. https://doi.org/10.1016/j.jrmge.2019.04.005

Lockner D (1993) The role of acoustic emission in the study of rock fracture. Int J Rock Mech Min Sci Geomech Abstr 30(7):883–899. https://doi.org/10.1016/0148-9062(93)90041-B

Ma TS, Peng N, Zhu Z, Zhang CB, Yang CH, Zhao J (2018) Brazilian tensile strength of anisotropic rocks: review and new insights. Energies 11(2):304. https://doi.org/10.3390/en11020304

Ma YF, Huang HY (2018) DEM analysis of failure mechanisms in the intact Brazilian test. Int J Rock Mech Min Sci 102:109–119. https://doi.org/10.1016/j.ijrmms.2017.11.010

Masri M, Sibai M, Shao JF, Mainguy M (2014) Experimental investigation of the effect of temperature on the mechanical behavior of Tournemire shale. Int J Rock Mech Min Sci 70:185–191. https://doi.org/10.1016/j.ijrmms.2014.05.007

Mokhtari M, Tutuncu AN (2016) Impact of laminations and natural fractures on rock failure in Brazilian experiments: a case study on Green River and Niobrara formations. J Nat Gas Sci Eng 36:79–86. https://doi.org/10.1016/j.jngse.2016.10.015

Moradian Z, Einstein HH, Ballivy G (2016) Detection of cracking levels in brittle rocks by parametric analysis of the acoustic emission signals. Rock Mech Rock Eng 49(3):785–800. https://doi.org/10.1007/s00603-015-0775-1

Park B, Min KB (2015) Bonded-particle discrete element modeling of mechanical behavior of transversely isotropic rock. Int J Rock Mech Min Sci 76:243–255. https://doi.org/10.1016/j.ijrmms.2015.03.014

Qiu JD, Li DY, Li XB (2017) Dynamic failure of a phyllite with a low degree of metamorphism under impact Brazilian test. Int J

Rock Mech Min Sci 94:10–17. https://doi.org/10.1016/j.ijrmms.2017.02.013

Roy DG, Singh TN (2016) Effect of heat treatment and layer orientation on the tensile strength of a crystalline rock under Brazilian test condition. Rock Mech Rock Eng 49(5):1663–1677. https://doi.org/10.1007/s00603-015-0891-y

Shen WQ, Shao JF (2015) A micromechanical model of inherently anisotropic rocks. Comput Geotech 65:73–79. https://doi.org/10.1016/j.compgeo.2014.11.016

Tan X, Konietzky H, Frühwirt T, Dan DQ (2015) Brazilian tests on transversely isotropic rocks: laboratory testing and numerical simulations. Rock Mech Rock Eng 48(4):1341–1351. https://doi.org/10.1007/s00603-014-0629-2

Tavallali A, Vervoort A (2010a) Effect of layer orientation on the failure of layered sandstone under Brazilian test conditions. Int J Rock Mech Min Sci 47(2):313–322. https://doi.org/10.1016/j.ijrmms.2010.01.001

Tavallali A, Vervoort A (2010b) Failure of layered sandstone under Brazilian test conditions: effect of micro-scale parameters on macro-scale behaviour. Rock Mech Rock Eng 43(5):641–653. https://doi.org/10.1007/s00603-010-0084-7

Tavallali A, Vervoort A (2013) Behaviour of layered sandstone under Brazilian test conditions: layer orientation and shape effects. J Rock Mech Geotech Eng 5(5):366–377. https://doi.org/10.1016/j.jrmge.2013.01.004

Tsang CF, Barnichon JD, Birkholzer J, Li XL, Liu HH, Sillen X (2012) Coupled thermo-hydro-mechanical processes in the near field of a high-level radioactive waste repository in clay formations. Int J Rock Mech Min Sci 49:31–44. https://doi.org/10.1016/j.ijrmms.2011.09.015

Valente S, Fidelibus C, Loew S, Cravero M, Iabichino G, Barpi F (2012) Analysis of fracture mechanics tests on opalinus clay. Rock Mech Rock Eng 45(5):767–779. https://doi.org/10.1007/s00603-012-0225-2

Vervoort A, Min KB, Konietzky H et al (2014) Failure of transversely isotropic rock under Brazilian test conditions. Int J Rock Mech Min Sci 70:343–352. https://doi.org/10.1016/j.ijrmms.2014.04.006

Wang J, Xie LZ, Xie HP, Ren L, He B, Li CB, Yang ZP, Gao C (2016) Effect of layer orientation on acoustic emission characteristics of anisotropic shale in Brazilian tests. J Nat Gas Sci Eng 36:1120–1129. https://doi.org/10.1016/j.jngse.2016.03.046

Wang PT, Cai MF, Ren FH (2018) Anisotropy and directionality of tensile behaviours of a jointed rock mass subjected to numerical Brazilian tests. Tunn Undergr Sp Technol 73:139–153. https://doi.org/10.1016/j.tust.2017.12.018

Winn K, Wong LNY, Alejano LR (2019) Multi-approach stability analyses of large caverns excavated in low-angled bedded sedimentary rock masses in Singapore. Eng Geol 259:105164. https://doi.org/10.1016/j.enggeo.2019.105164

Wong LNY, Jong MC (2014) Water saturation effects on the Brazilian tensile strength of gypsum and assessment of cracking processes using high-speed video. Rock Mech Rock Eng 47(4):1103–1115. https://doi.org/10.1007/s00603-013-0436-1

Xia YJ, Zhou H, Zhang CQ, He SH, Gao Y, Wang P (2019) The evaluation of rock brittleness and its application—a review study. Eur J Environ Civ En. https://doi.org/10.1080/19648189.2019.1655485

Xia YJ, Zhang CQ, Zhou H, Chen JL, Gao Y, Liu N, Chen PZ (2020) Structural characteristics of columnar jointed basalt in drainage tunnel of Baihetan hydropower station and its influence on the behavior of P-wave anisotropy. Eng Geol. https://doi.org/10.1016/j.enggeo.2019.105304

Xu GW, He C, Chen ZQ, Su A (2018) Transverse isotropy of phyllite under brazilian tests: laboratory testing and numerical simulations. Rock Mech Rock Eng 51(4):1111–1135. https://doi.org/10.1007/s00603-017-1393-x

Yang SQ, Yin PF, Huang YH (2019) Experiment and discrete element modelling on strength, deformation and failure behaviour of shale under Brazilian compression. Rock Mech Rock Eng 52:4339–4359. https://doi.org/10.1007/s00603-019-01847-z

Yin PF, Yang SQ (2018) Experimental investigation of the strength and failure behavior of layered sandstone under uniaxial compression and Brazilian testing. Acta Geophys 66(4):585–605. https://doi.org/10.1007/s11600-018-0152-z

Zhang SW, Shou KJ, Xian XF, Zhou JP, Liu GJ (2018) Fractal characteristics and acoustic emission of anisotropic shale in Brazilian tests. Tunn Undergr Sp Technol 71:298–308. https://doi.org/10.1016/j.tust.2017.08.031

Zhou H, Liu HT, Hu DW, Yang FJ, Lu JJ, Zhang F (2016) Anisotropies in mechanical behaviour, thermal expansion and P-wave velocity of sandstone with bedding planes. Rock Mech Rock Eng 49(11):4497–4504. https://doi.org/10.1007/s00603-016-1016-y

Zuo JP, Lu JF, Ghandriz R, Wang JT, Li YH, Zhang XY, Li J, Li HT (2020) Mesoscale fracture behavior of Longmaxi outcrop shale with different bedding angles: experimental and numerical investigations. J Rock Mech Geotech Eng 122(2):297–309. https://doi.org/10.1016/j.jrmge.2019.11.001